Cellulose Derivative and Polyionic Liquid Crosslinked Network Gel Electrolytes for Sodium Metal Quasi-Solid-State Batteries

Shuzhi Zhao, Yixing Shen, Haiying Che, Maher Jabeen, Chu Lu, Xiao-Zhen Liao,* and Zi-Feng Ma*

Sodium metal batteries have gained attention as a potential solution to the low energy densities presented by current sodium-ion batteries. However, the commonly available electrolyte systems usually fall short in safety performance. Gel polymer electrolytes, closely resembling liquid electrolytes, offer a promising balance of performance and developmental potential. A proposed polymer plastic-crystal ionic gel composite electrolyte, featuring a polycation auxiliary chain, innovatively copolymerizes ionic liquid cations with electrolyte additives. These auxiliary chains crosslink with the main chain, attracting anions from the ionic liquid and sodium salts. Both experimental evidence and theoretical calculations affirm that this electrolyte exhibits high cation transference numbers and significant mean square displacement radii. By facilitating uniform sodium ion migration, the electrolyte has powered sodium symmetrical cells for over 550 h and has supported stable cycling of $Na_3V_2(PO_4)_3$ (NVP)-sodium metal batteries at a 1 C rate for more than 800 cycles. These achievements underscore its potential in advancing the development of condensed-state sodium metal batteries.

1. Introduction

Lithium-ion batteries are integral to modern technology, powering devices from mobile phones to electric vehicles. However, the cost and uneven global distribution of lithium and other critical metals like cobalt have spurred interest in sodium-ion batteries.[1] Sodium-ion batteries, similar in design and

manufacturing to lithium-ion variants, offer superior rate and low-temperature performance, though they currently suffer from lower energy density.[2] Sodium metal is an especially promising anode material for these batteries due to its low potential (−2.71 V vs standard hydrogen) and high specific capacity (1166 mA h g^{-1}).[3] Despite their potential, sodium-ion batteries face challenges with current electrolyte systems, which can react with sodium metal anodes.[4] These reactions consume large amounts of electrolytes, produce gas, and lead to the formation of sodium dendrites that can cause short circuits by piercing the separator.[5] The use of toxic, flammable, and leak-prone organic solvents in these electrolytes further increases safety risks.[6]

Solid electrolytes, both inorganic and polymer-based, are emerging as solutions due to their stable chemical and electrochemical properties and mechanical strength, making them suitable for use with

sodium metal anodes.[7] Inorganic solid electrolytes, however, can be rigid, leading to poor contact at the electrode interface.[8] Polymer solid electrolytes, in contrast, are more flexible and provide better contact due to their plasticity. While pure solid polymer electrolytes have low ionic conductivity, making them less practical, gel polymer electrolytes (GPEs) offer higher conductivity, good plasticity, and sufficient mechanical strength, positioning them as a viable option for sodium metal batteries.[9] Nonetheless, challenges remain, including leakage of organic solvents and uneven metal surface deposition, primarily due to low cation transference numbers, which limit their broader application in sodium metal batteries.[10] It has taken many efforts to synthesize stable GPE directly, rather than soaking the polymer matrix in a liquid electrolyte so that the liquid component is completely stable within the polymer framework.[11] In spite of this, due to the reduction in the liquid composition to mass ratio, the resulting ionic conductivity of GPEs is low, and the interface contact is also problematic. Furthermore, the safety of GPEs cannot be guaranteed.[12] Consequently, flame retardant and non-volatile ionic liquids are used to replace the solvent portion of GPEs, thereby further improving the ionic conductivity and safety of the electrolytes.[13] Research has been conducted on GPEs containing ionic liquid in order to achieve good application scenarios.

S. Zhao, Y. Shen, C. Lu, X.-Z. Liao, Z.-F. Ma
Shanghai Electrochemical Energy Devices Research Center
Department of Chemical Engineering
Shanghai Jiao Tong University
Shanghai 200240, China
E-mail: liaoxz@sjtu.edu.cn; zfma@sjtu.edu.cn
Y. Shen, H. Che, M. Jabeen, Z.-F. Ma
Zhejiang Natrium Energy Co. Ltd.
Shaoxing 312300, China
Y. Shen, Z.-F. Ma
Shaoxing Research Institute of Renewable Energy and Molecular
Engineering Shanghai Jiao Tong University
Shaoxing 312300, China

The ORCID identification number(s) for the author(s) of this article can be found under https://doi.org/10.1002/adfm.202422162

DOI: 10.1002/adfm.202422162

**ADVANCED
SCIENCE NEWS**

www.advancedsciencenews.com

**ADVANCED
FUNCTIONAL
MATERIALS**

www.afm-journal.de

According to Tiago et al., their application of C_{3m}PyrFSI and NaFSI in combination with PVDF-HFP polymer to form GPE achieved a specific capacity of 83 mAh g^{-1} at a 1 C charge–discharge rate of $Na_3V_2(PO_4)_3$ (NVP)–sodium metal battery, and a capacity retention rate of 92% after 150 cycles.[6b] Furthermore, Jun et al. used the electron-rich Nerolin additive to enhance salt ionization in GPE composed of PVDF-HFP, NaTFSI, and EmimFSI, as well as to inhibit cation movement in the ionic liquid. As a result, an ion transference number of 0.79 was obtained in the electrolyte and an excellent cycle performance and rate performance were obtained in the NVP–sodium metal battery.[14] Despite some research progress in GPE, its poor mechanical properties and ionic conductivity still need to be improved, as well as the sustainability of resources. Cellulose triacetate (CTA), a readily available cellulose derivative, is known for its robust mechanical properties and chemical stability, as well as a high dielectric constant that promotes ion dissociation.[15] Membranes based on CTA have been widely utilized in applications such as water treatment and gas separation.[16] While CTA has been explored in lithium-ion battery polymer electrolytes, its applications in sodium-ion batteries have been less examined.[17] Previously, we developed a CTA-based polymer ionic gel polymer electrolyte that facilitated stable cycling of sodium metal batteries at elevated temperatures, although its room temperature performance was suboptimal.[18] Plastic crystals are solid crystals that have plasticity, typically small organic molecules with high polarity.[19] Because the crystal has a low molecular rotation potential barrier, even though the intermolecular arrangement still maintains the periodicity of the 3D lattice and can maintain its basic characteristics, the crystal is still able to maintain its periodicity due to the low molecular rotation potential barrier. The rotation of the molecule at equilibrium causes orientation disorder, which facilitates intermolecular sliding and contributes to the plasticity of the crystal. Thus, plastic crystals have been applied to enhance ionic conductivity and, on the other hand, can promote salt dissociation by coordinating with alkali metal ions.[20] So far, succinonitrile (SN) is the most widely used and frequently used plastic crystal.

In our current study, we introduce a plastic-crystal composite gel polymer electrolyte (PCGPE) featuring CTA as the primary chain and a polyionic liquid as the crosslinking agent. This configuration offers enhanced mechanical strength and flexibility. Unlike a GPE that is formed by soaking the polymer matrix in the electrolyte under normal circumstances, the electrolyte film behaves as a no-free-liquid form, with no liquid on the surface and no liquid leakage when heated or compressed, which minimizes the risk of liquid leakage to a large extent. The polyionic liquid, embodying both ionic and polymer properties, stabilizes cations within the network and attracts charges from its anions and those in the sodium salts, improving sodium ion migration. This enhancement leads to higher cation transference numbers and promotes more uniform sodium deposition and stripping on the metal surface. Employing this PCGPE, significant performance has been achieved: a specific capacity exceeding 100 mAh g^{-1} at a 1 C rate with an NVP cathode at 30 °C, maintaining 80.0% capacity retention over 790 cycles. Additionally, cycled at a current density of 0.05 mA cm^{-2}, the Na symmetric cell cycled over 550 h. These results underscore the potential of this novel electrolyte in advancing sodium metal battery technology.

2. Results and Discussion

Figure 1 illustrates the synthesis process for the PCGPE. The procedure begins with the preparation of a solution containing 1-Allyl-3-methylimidazolium chloride (AMImCl and sodium bis(trifluoromethylsulfonyl)imide (NaTFSI) in acetonitrile, where an anion exchange reaction produces AMIMTFSI and NaCl. This resultant solution is then mixed with a CTA solution in dichloromethane (DCM) at a predetermined ratio. To this mixture, SN and vinylene carbonate (VC) are added to achieve a homogeneous solution. Following the incorporation of the photoinitiator 2-hydroxy-2-methylpropiophenone (HMPP), the solution is exposed to UV light, turning it yellow as polymerization occurs. The resulting composition includes CTA, polymerized p(AMImcoVC), SN, and NaTFSI, and is named pAMIm for use. The mixture is then poured onto a flat PTFE surface and covered with a glass plate, allowing for the slow evaporation of the solvents. After 24 h, the solvents have sufficiently evaporated, and the semi-solid film is carefully peeled from the surface. The film undergoes a final drying process in a vacuum oven at 50 °C for 6 h, resulting in the ready-to-use PCGPE. This material is noted for its potential applications in sodium metal batteries due to its enhanced ionic conductivity and mechanical stability. In this structure, CTA serves as the main backbone, taking advantage of its strong mechanical properties. Several oxygen groups are present in CTA, which actively interact with sodium ions. As a result of these interactions, Na ions are transported and dissociated more efficiently, which is essential to the efficient operation of batteries.

Crosslinked to the CTA main chain is p(AMImcoVC), which serves to anchor nitrogen cations along the polymer chain. The cross-linking of the electrolyte plays a critical role in its structural stability and ionic functionality. Through electrostatic forces, TFSI anions are attracted to p(AMImcoVC) chains. As a result of this arrangement, concentration polarization is greatly mitigated by minimizing anion mobility, thereby promoting a more uniform distribution of the electric field within the electrolyte. A high degree of uniformity enhances interfacial stability and prevents the growth of dendrites, which are detrimental to battery performance and safety.

Additionally, a PCGPE that utilizes conventional ionic liquids was also synthesized which does not involve a polymerization process and is named PyR14.

In the study of the PCGPE, a non-polymerizable ionic liquid, PyR_{14}TFSI, as a comparison to assess electrochemical performance and other physical properties was included. Infrared spectroscopy results depicted in **Figure 2c** reveal that after UV exposure, the absorption peaks at 1833 and 1800 cm^{-1}, correspond to the double bond absorptions of AMIm and VC vanished. This indicates the successful polymerization of AMIm and VC within the electrolyte, with a noticeable blue shift in peaks due to the electron-withdrawing effects from cationic aromatic rings or oxygen groups attached to these double bonds.

An X-ray diffraction (XRD) analysis is an important tool for determining a sample's crystal structure. Previously, Hindeleh et al. analyzed the crystallinity of CTA crystallized after heat treatment at different temperatures based on the XRD pattern analysis of CTA.[21] As can be seen from Figure 2a, the analytical
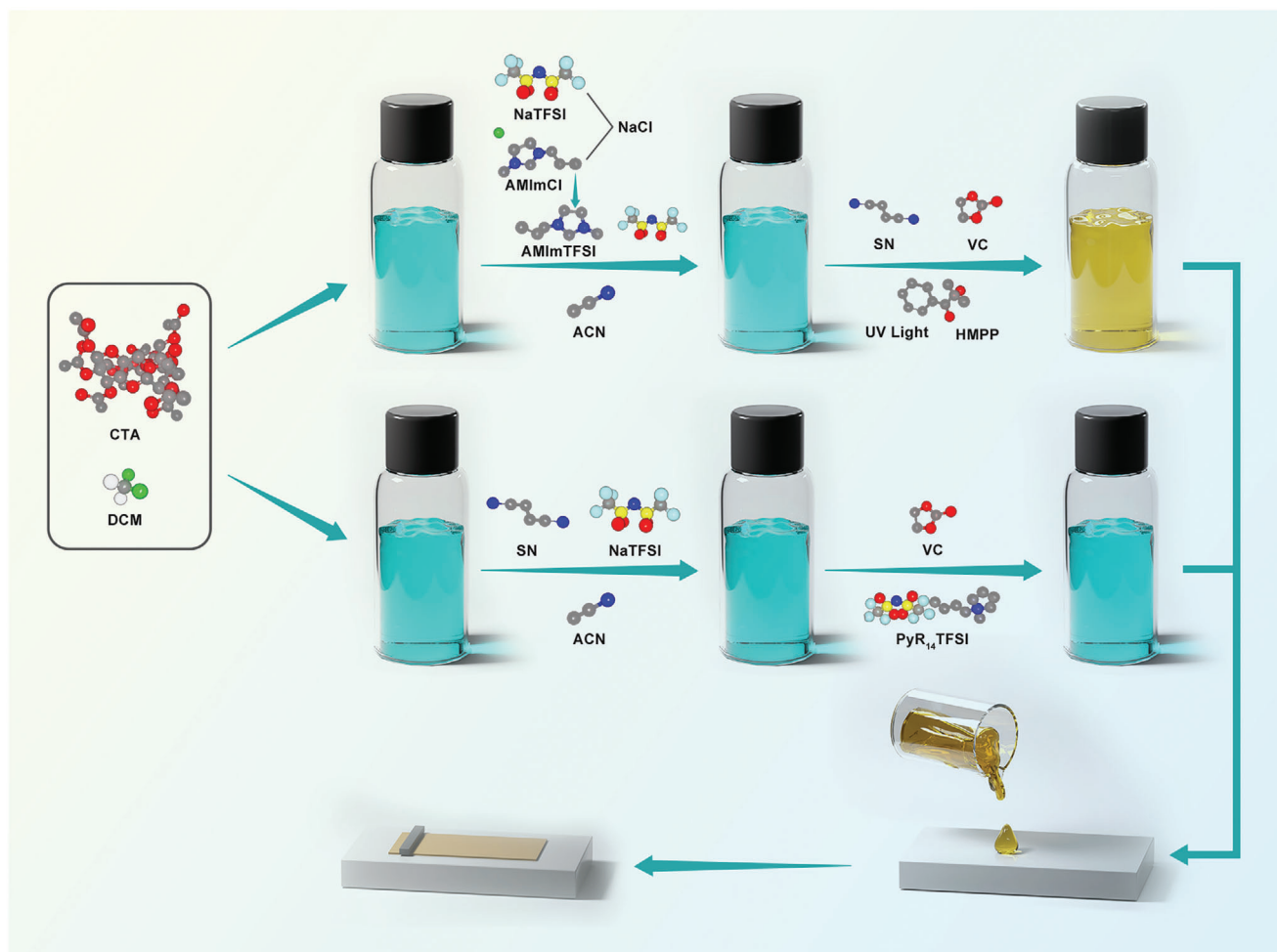
Figure 1. Preparation route of PCGPEs.

processing results of PyR14 indicate that its peaks correspond to the crystal faces (210), (111), and (320) of CTA crystals. Based on the XRD results of pAMIm, its peaks correspond to the crystal faces of CTA (110), (210), (111), (410), and (320). In terms of the diffraction peak intensity of (111) crystal plane, pAMIm has a slightly stronger signal than PyR14, and it has a slightly stronger crystallinity because it has more crystal plane peaks. By testing the strain–stress curves of pAMIm and PyR14, it is found that pAMIm has a higher fracture stress ($\approx$0.2 MPa) and a higher strain ($\approx$10%), as shown in Figure S3 (Supporting Information) demonstrated stronger mechanical properties than PyR14 (less than 0.1MPa and $\approx$6%). Auxiliary chains obtained by copolymerization can also contribute to the mechanical strength of pAMIm PCGPE, in addition to CTA polymer.

A thermogravimetric analysis (TGA) in Figure 2b indicates that both pAMIm and AMIm show slightly lower thermal stability when compared to PyR14, beginning to decompose $\approx$50 °C earlier. In this case, the reduced stability may be attributed to the plasticizing effect of the AMIm ionic liquid on the CTA chain, which makes the chain more susceptible to degradation.[22] No-

tably, pAMIm displays slightly improved thermal stability over AMIm, correlating with the polymerization effect of the liquid component in the AMIm PCGPE system. These changes result from the cross-linking effect between the ionic liquid polymerization and the CTA backbone. The primary thermal decomposition peak at 285 °C corresponds to the decomposition of the main CTA chain. For PyR14, the decomposition peak at 414 °C corresponds with the decomposition temperature of the $PyR_{14}TFSI$ ionic liquid. In the AMIm and pAMIm samples, no distinct peaks for ionic liquid decomposition were noted, but the mass loss at 285 °C was more pronounced than in PyR14, suggesting some decomposition of the ionic liquid due to interaction with CTA. The final decomposition peak at 439 °C is attributed to NaTFSI.[23]

A minor endothermic peak $\approx$32 °C observed in the differential scanning calorimetry (DSC) graph, Figure S1 (Supporting Information), could indicate the melting of pAMIm polymer chains. The endothermic peak at 180 °C corresponded with the melting of CTA polymer chains. In an ignition test using a polyethylene (PE) separator and commercial electrolyte, the electrolytes showed high flammability when exposed to an open flame with
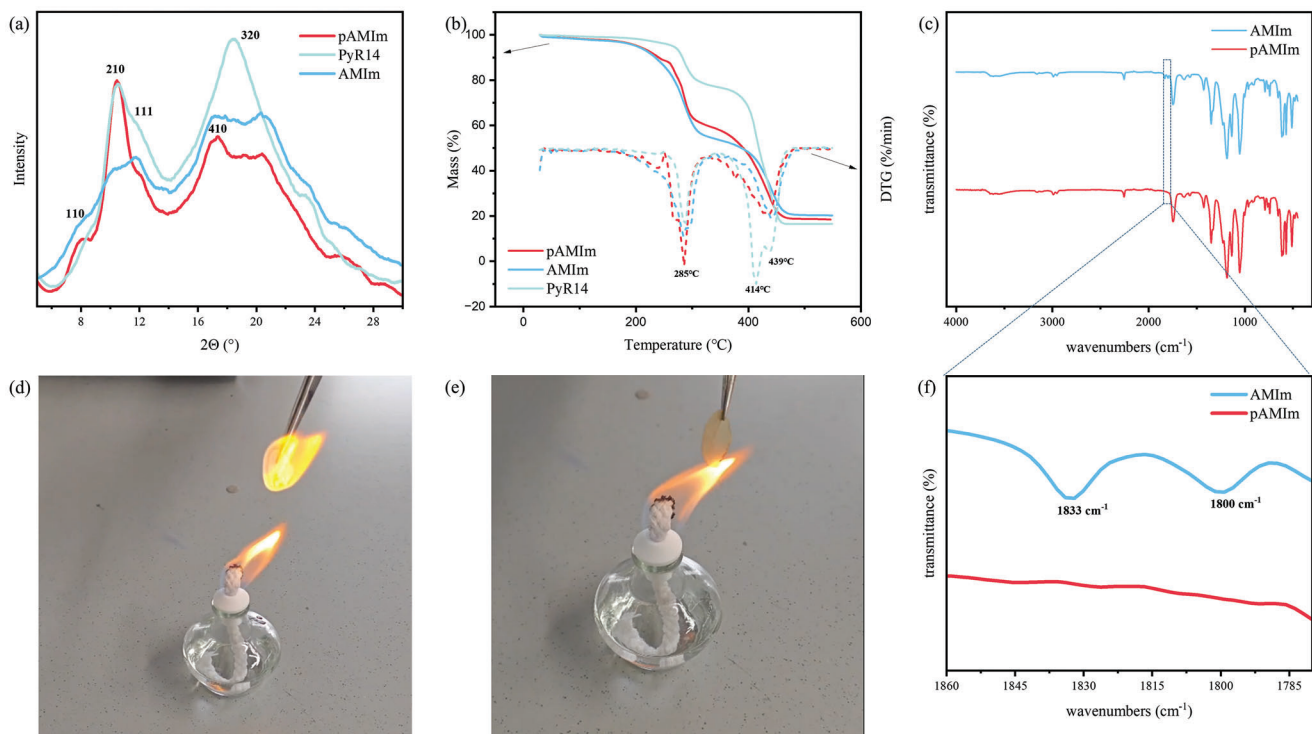
Figure 2. a) XRD spectra of pAMIm, AMIm, and PyR14 PCGPE; b) TGA and dTG curves of pAMIm, AMIm, and PyR14 PCGPE; c) FT-IR spectra of pAMIm and AMIm PCGPE, with magnification (f); d,e). flammability test of the liquid electrolyte and PCGPE.

continuous intense burning. The pAMIm electrolyte film, however, eventually charred, but did not ignite, demonstrating significantly improved safety when compared to traditional electrolytes and separators.

Quantum chemical calculations were first performed to optimize molecular geometries and frequencies of the CTA chain, p(AMImcoVC) chain, PyR_{14}^+ cation, $TFSI^-$ anion, VC molecule, and SN molecule using the Gaussian 16 package at B3LYP/6-31g(d) level of theory.[24] The electrostatic potential (ESP) figures of different molecules further used are shown in Figures S5–S7 (Supporting Information). It can be seen from ESP results that the p(AMImcoVC) chain contains imidazole centers with a relatively concentrated positive charge (labeled N^+ center), and in the TFSI anion, the negative charge is relatively concentrated in the oxygen group. The added SN has a great polarity and promotes the release of sodium ions from anion bondage. Results from ab initio molecular dynamics (AIMD) simulations highlight significant enhancements in the mobility of sodium atoms with the incorporation of pAMIm chains, noting an increase in their mobility range from 0 picoseconds (ps) to 2 ps. The simulation was conducted on ORCA under the r^2SCAN-3c level of theory.[25] The temperature was controlled with canonical sampling through a velocity rescaling (CSVR) thermostat at 298.15 K for 2000fs with one step of 1fs. Based on the simulation results, the Na-N spacing for NaTFSI is optimized by Gaussian to 3.57 Å at 0ps. The Na-N spacing in NaTFSI is slightly reduced to 3.46 Å after a 2-ps dynamic simulation. When combined with pAMIm, however, the Na-N distance in NaTFSI expanded to 6.87 Å after 2ps dynamic simulation, which is consistent with the hypothesis that the pAMIm cochain promotes the dissociation of NaTFSI.

In the time range of 2ps, the sodium ions in the pAMIm model have a larger mobile range than the sodium ions in NaTFSI, in other words, it is easier to decoupage from the TFSI anion and bind to SN. Molecule dynamic simulations from GROMACS further elucidate this finding, showing that within a 10 nanosecond (ns) timeframe, the mean square displacement (MSD) for pAMIm exceeds that of PyR14.[26] Correspondingly, diffusion coefficients derived from these simulations indicate that pAMIm (5.5924) supports faster sodium ion diffusion compared to PyR14 (2.6735).

Figure 3d,h provide additional insights, illustrating that in the pAMIm system, sodium ions predominantly coordinate with SN, whereas in PyR14, sodium coordination occurs more frequently with corresponding anions. In Figure 3d, the snapshot of molecular dynamic simulation from GROMACS demonstrates intuitively the difference in the coordination environment of sodium ions. The enlarged local structure from PyR14 and pAMIm showed that the main ligands around sodium ions are TFSI anion and SN. This result is consistent with the coordination relationship between SN and Na ions obtained in Figure 3h. It illustrates that the SN ligands in pAMIm and PyR14 PCGPE are arranged in a bilayer structure, exhibiting inner coordination numbers of 0.8 and 0.5, respectively, and overall coordination numbers of ≈4.0 and 3.0. This suggests that in pAMIm PCGPE, the sodium ions are predominantly coordinated with SN ligands, with minimal involvement of TFSI anions. Conversely, in PyR14 PCGPE, the lower SN coordination number indicates a significant likelihood of TFSI anions participating in the coordination. This anion coordination in PyR14 leads to clustering, which poses challenges and results in greater polarization under high current densities. Ionic
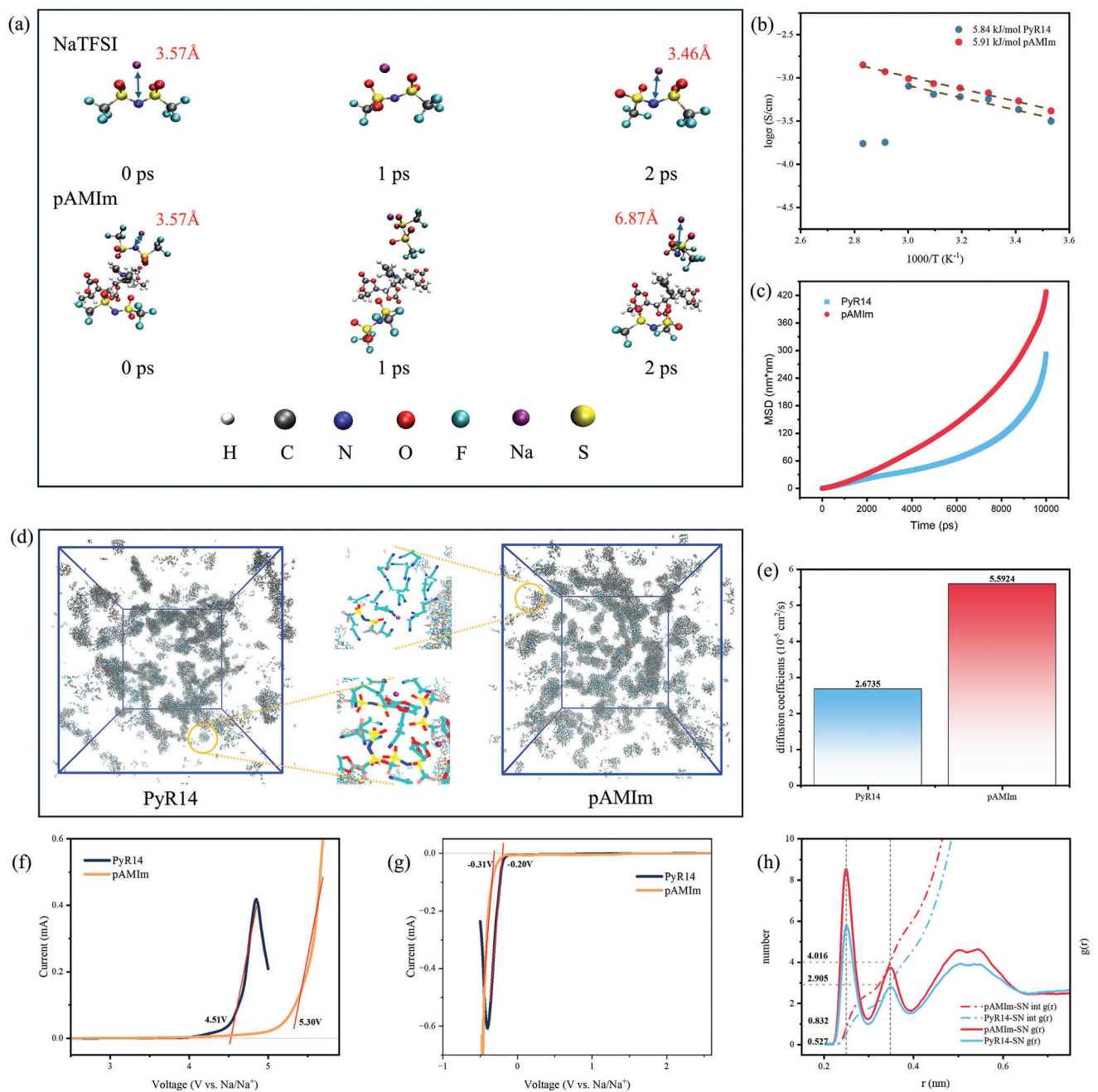
ADVANCED
SCIENCE NEWS

www.advancedsciencenews.com

ADVANCED
FUNCTIONAL
MATERIALS

www.afm-journal.de

Figure 3. a) Molecular structure of NaTFSI and pAMIm before DFT-MD simulation (0 ps) and after simulation (1 ps and 2 ps); b) Ionic conductivity of pAMIm and PyR14 PCGPE; c) The mean square displacement and e) diffusion coefficients of Na$^+$ in pAMIm and PyR14 electrolytes; d) Snapshot of molecular dynamics simulation of pAMIm and PyR14 electrolytes; f,g) LSV curves of pAMIm and PyR14 electrolytes. h) Coordination number of Na$^+$ with SN in pAMIm and PyR14 electrolytes.

conductivity tests further support the data from molecular dynamics simulations, indicating that pAMIm (6.72×10^{-4} S cm^{-1}) achieves slightly higher ionic conductivity than PyR14 (5.70×10^{-4} S cm^{-1}). Notably, at elevated temperatures (60 °C), PyR14 exhibits a decrease in ionic conductivity due to instability in its electrolyte film, characterized by liquid exudation. In contrast, the pAMIm electrolyte, by copolymerizing ionic liquid cations with VC and forming a crosslinked structure, stabilizes SN within

the polymer network, enhancing its thermal stability. Furthermore, electrochemical tests reveal that pAMIm has a higher electrochemical window (5.30V) compared to PyR14 (4.51V). This superiority is attributed to the stable crosslinked polymer network in pAMIm, which effectively prevents oxidation of SN or VC at the cathode surface, thereby enhancing the overall stability and performance of the electrolyte under various operational conditions.

The impedances of pAMIm and PyR14 PCGPE before and after chronoamperometry experiments can be determined by fitting **Figure 4b**. The impedance of pAMIm before and after the chronoamperometry experiment was 905.2 and 990.6 Ω, respectively. PyR14 has an impedance of 4887 Ω before and after the chronoamperometry experiment of 4920 Ω. Ion transference number measurements show that the pAMIm electrolyte has a significantly higher ion transference number (0.726) compared to PyR14 (0.535). This finding aligns with our molecular dynamics simulations, which suggest that pAMIm effectively restricts the transmission and movement of most TFSI anions through the charge attraction of cations.

The stability of sodium metal with the PCGPE was evaluated using symmetric sodium metal batteries. In Figure 4c, the pAMIm electrolyte enabled the symmetric battery to operate successfully for over 550 h under a current density of 0.05 mA cm^{-2}. By contrast, the PyR14 electrolyte showed signs of interface deterioration after just over 150 h. With pAMIm, this enhanced performance can be attributed to its higher cation transference number, which facilitates uniform ion deposition and stripping at the electrolyte-sodium metal interface, which is essential to the long-term stability of the battery. It can also be seen in Figure S14 (Supporting Information) that the sodium-symmetric battery with pAMIm PCGPE and 0.1 mA cm^{-2} current density cycled smoothly for more than 250 h.

Scanning Electron Microscopy (SEM) observations of the sodium metal surfaces after 100 h of operation in symmetric batteries further illustrate these differences. As seen in the surface morphology of SEM images, the sodium metal surface is relatively flat and uniform when pAMIm PCGPE is used, and its poor electrical conductivity indicates an organic-rich layer. As opposed to PyR14 PCGPE, which presents strike-shaped bumps and exposed sodium metal of varying sizes on the sodium metal surface. Dendrites begin to form on the sodium metal surface when a basic 1m NaPF6 in EC/PC electrolyte (BASE) is used. Compared with PyR14 and BASE, pAMIm PCGPE exhibits more uniform sodium ion migration, and a small amount of TFSI anion in the solvation structure promotes uniform SEI formation. As a result of uneven sodium ion migration and a large amount of TFSI anions in the solvation structure, PyR14 PCGPE produces uneven deposition structures on the surface of sodium metal.

Figure 5a–c illustrates the charge-discharge performance of sodium metal batteries using NVP cathodes and different electrolytes, evaluated at a 1C rate with a pre-cycling at a 0.1C rate for two cycles. The pAMIm PCGPE demonstrates superior discharge capacity and cycling stability compared to PyR14 and commercial liquid electrolytes. The initial charge–discharge curves for batteries assembled under PCGPE conditions reveal a dual voltage plateau, suggesting an incomplete formation of the solid electrolyte interface (SEI) layer and discontinuous interface contact between the gel electrolyte and sodium metal in early cycles. In the long-cycle test of charge and discharge at 1 C rate, pAMIm PCGPE has the highest initial specific capacity, reaching 105.9 mAh g^{-1}. The initial specific capacity of PyR14 PCGPE and the electrolyte has a small difference, but both are smaller than that of pAMIm PCGPE. 92.3 and 90.5 mAh g^{-1}, respectively. By the 50th cycle, both PyR14 and commercial electrolytes exhibit notable capacity reductions, while the pAMIm electrolyte maintains ≈99% capacity retention. Impressively, by the 200th

cycle, pAMIm sustains 89.8% capacity retention, significantly outperforming PyR14 and commercial electrolytes, which maintain only 74% and 26.3% respectively. To evaluate the long-cycle performance of the pAMIm-based PCGPE electrolyte, NVP cathode material, and sodium metal anode material were used to test the battery for charge and discharge cycles at 1 C and 30 °C and the quasi-solid-state battery maintained 80% capacity retention at 780 cycles, which was shown in Figure S16 (Supporting Information).

SEM images taken after 200 cycles were used to further investigate the surface of sodium metal after cycling a long-term range at 1 C rate, as shown in Figure 5e,f, indicating that the sodium surface with pAMIm was smoother. As demonstrated by EDS analysis, sodium and sulfur elements, which are derived from TFSI anions, were evidently observed on the surface of sodium metal using PyR14 PCGPE. This indicates that sodium dendrites are formed during the deposition process, and the area of TFSI anion reduction makes sodium deposition at this site more difficult. This irregularity in the SEI layer and surface deposits leads to regions that are impervious to sodium ion passage, causing localized sodium deposition and uneven surfaces. Such conditions exacerbate exposure to sodium metal, precipitating battery failure. A uniform distribution of sodium elements can be observed on the surface of sodium metal using pAMIm PCGPE, while a small concentration of other elements can also be observed in the surface gaps due to the reduction of free mobile anions as a result of polyionic liquid cation attraction. In the solvated layer, only a small amount of TFSI anions are reduced by the co-deposition of Na ions to form stable SEI. Figures S9 and S10 (Supporting Information) show the SEM images of the NVP cathode material cycled at 1C using PyR14 and pAMIm PCGPE, respectively. It can be observed from the figures that the NVP cathode material using pAMIm PCGPE has more complete NVP pellets and a more uniform binder distribution. On the contrary, the NVP cathode material using PyR14 PCGPE is more fragmented, and the binder is unevenly distributed. Compared with Figure S8 (Supporting Information), which exhibited the NVP cathode material before cycling, the cathode with pAMIm PCGPE was more intact. This is also one of the reasons why the capacity of NVP-Na cells utilizing PyR14 PCGPE plunged at 200 cycles.

Additional rate capability tests with NVP-sodium metal batteries, ranging from 0.1 to 2 C, reveal that batteries using the pAMIm electrolyte achieve a capacity of 106.0 mAh g^{-1} at 0.1 C and maintain 95.1 mAh g^{-1} at 2 C, with a capacity retention rate of 89.7%. Conversely, the PyR14 electrolyte, while starting at a slightly higher capacity of 106.5 mAh g^{-1} at 0.1 C, drops to 79.6 mAh g^{-1} at 2 C, with a retention rate of 74.7%, underscoring that the polycation auxiliary chain in pAMIm significantly boosts rate performance. In addition, it can be seen that the coulomb efficiency of pAMIm PCGPE is higher than that of PyR14 in the magnification performance test. This is related to the smooth and stable SEI layer formed by pAMIm PCGPE, while PyR14 PCGPE leads to decomposition and reorganization of SEI.

Figure 5h depicts a flexible pouch battery setup, which after charging, powers a signboard effectively. Despite undergoing folding and cutting operations, the battery continues to discharge without any safety incidents such as fire or smoke, demonstrating its reliability and safety. This level of performance and stability in the pAMIm electrolyte highlights its potential for
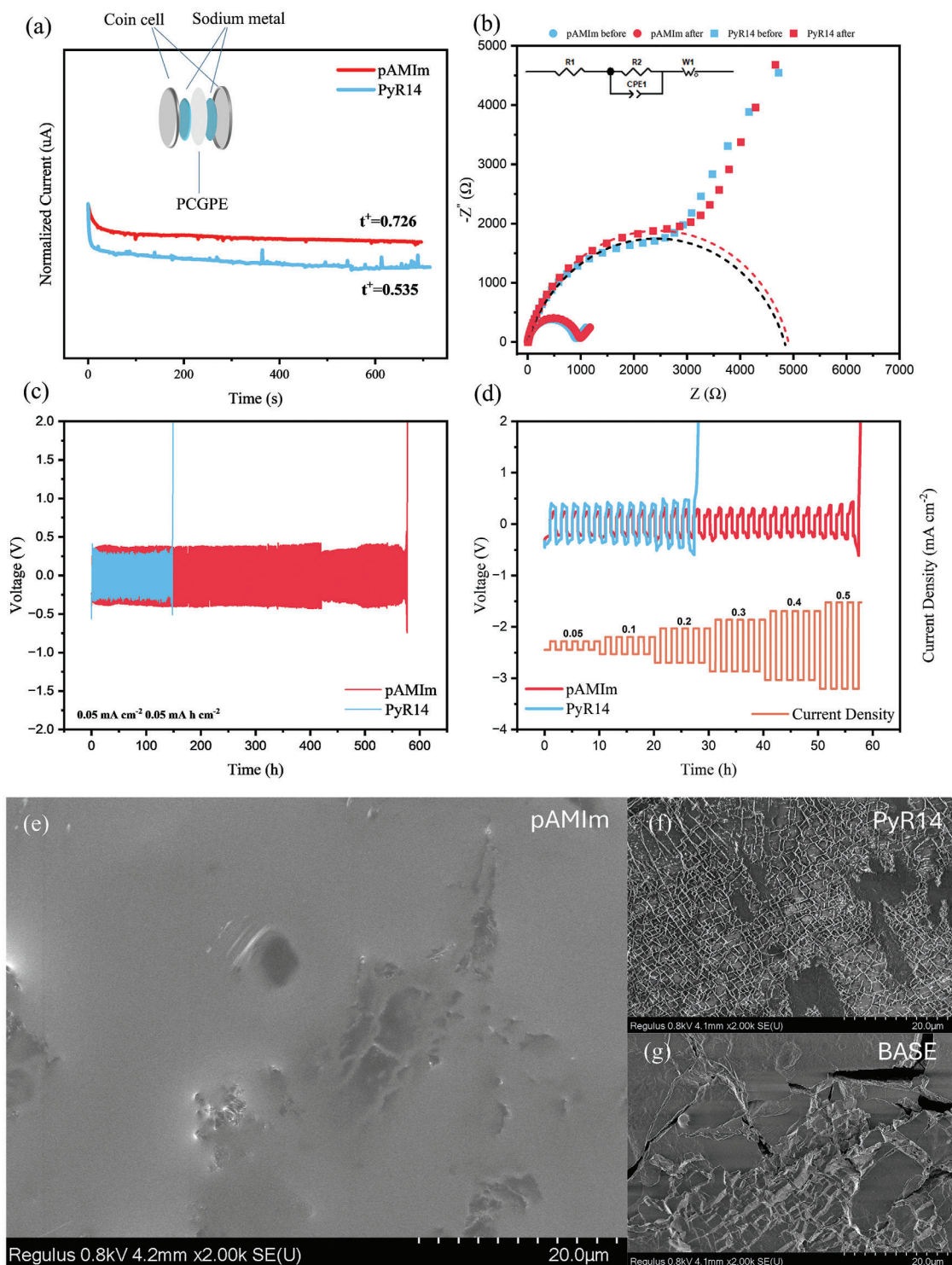
**ADVANCED
SCIENCE NEWS**

www.advancedsciencenews.com

**ADVANCED
FUNCTIONAL
MATERIALS**

www.afm-journal.de

Figure 4. a) The current–time curve of the Na symmetric cell using pAMIm or PyR14 as PCGPE with simultaneous illustration; b) Electrochemical impedance spectroscopy (EIS) spectra of the Na symmetric cell using pAMIm or PyR14 as PCGPE before and after the chronoamperometry test; c) Comparison of cycling performance of Na symmetric cells with pAMIm or PyR14 at 0.05 mA cm^{-2}; d) Voltage profiles of repeated Na plating/stripping in symmetric cells with different current densities; e–g) SEM figures of cycled Na surface with pAMIm, PyR14 and liquid electrolyte, separately.
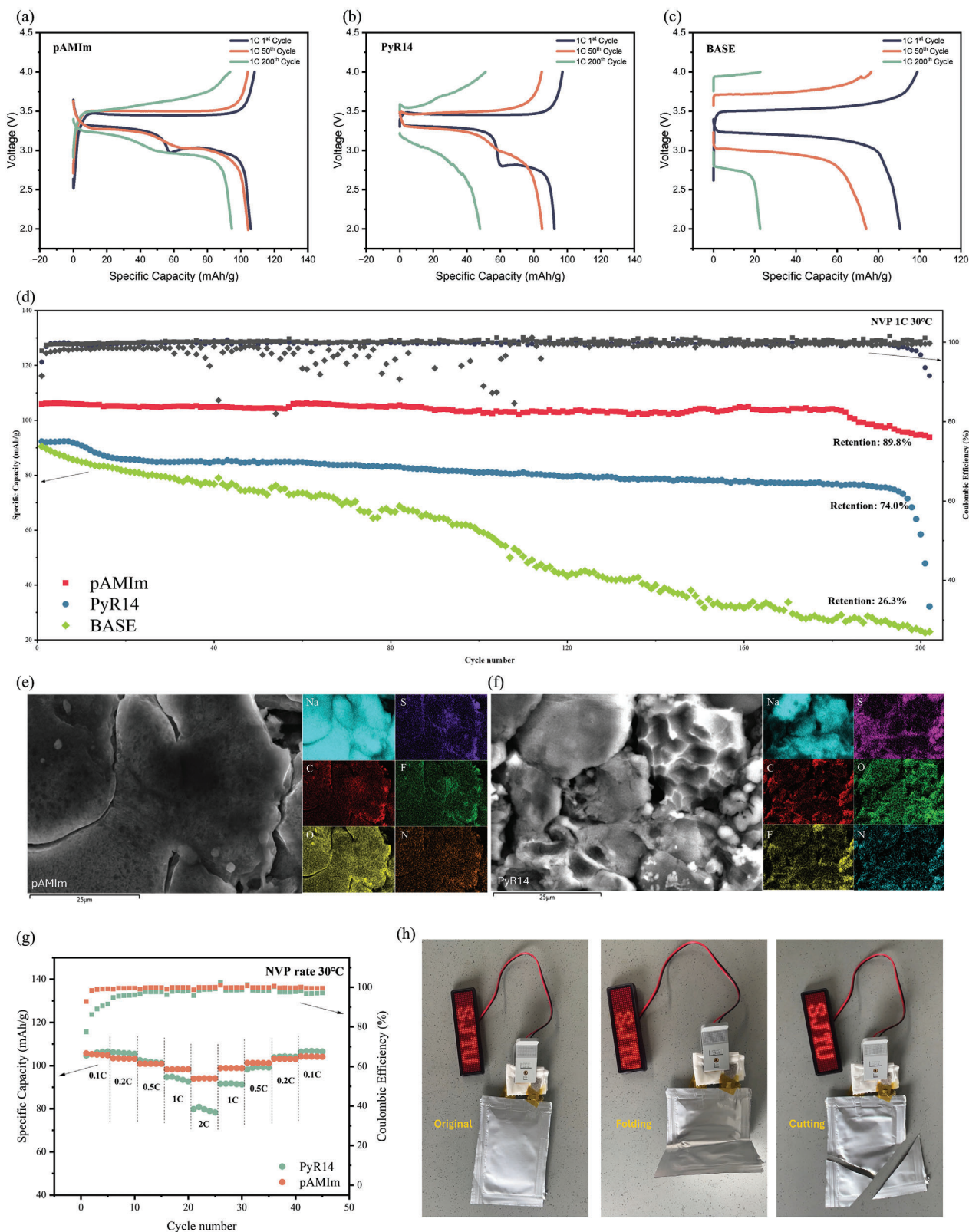
**ADVANCED
SCIENCE NEWS**

www.advancedsciencenews.com

**ADVANCED
FUNCTIONAL
MATERIALS**

www.afm-journal.de

Figure 5. Charge/discharge curves at 1, 50, and 200 cycles of solid-state NVP/ Na cells using a) pAMIm, b) PyR14, and c) liquid electrolyte at 1 C, 30 °C, respectively; d) Cycling performance of NVP/Na cells with pAMIm, PyR14 and liquid electrolyte at 1 C, 30 °C; e,f) SEM and EDS spectra of sodium surfaces cycled with pAMIm and PyR14; g) Rate performance of NVP/ Na cells using pAMIm and PyR14 PCGPE from 0.1 to 2 C, 30 °C; h) Illustration of NVP-Na pouch cells lighting a light board.

**ADVANCED
SCIENCE NEWS**

www.advancedsciencenews.com

**ADVANCED
FUNCTIONAL
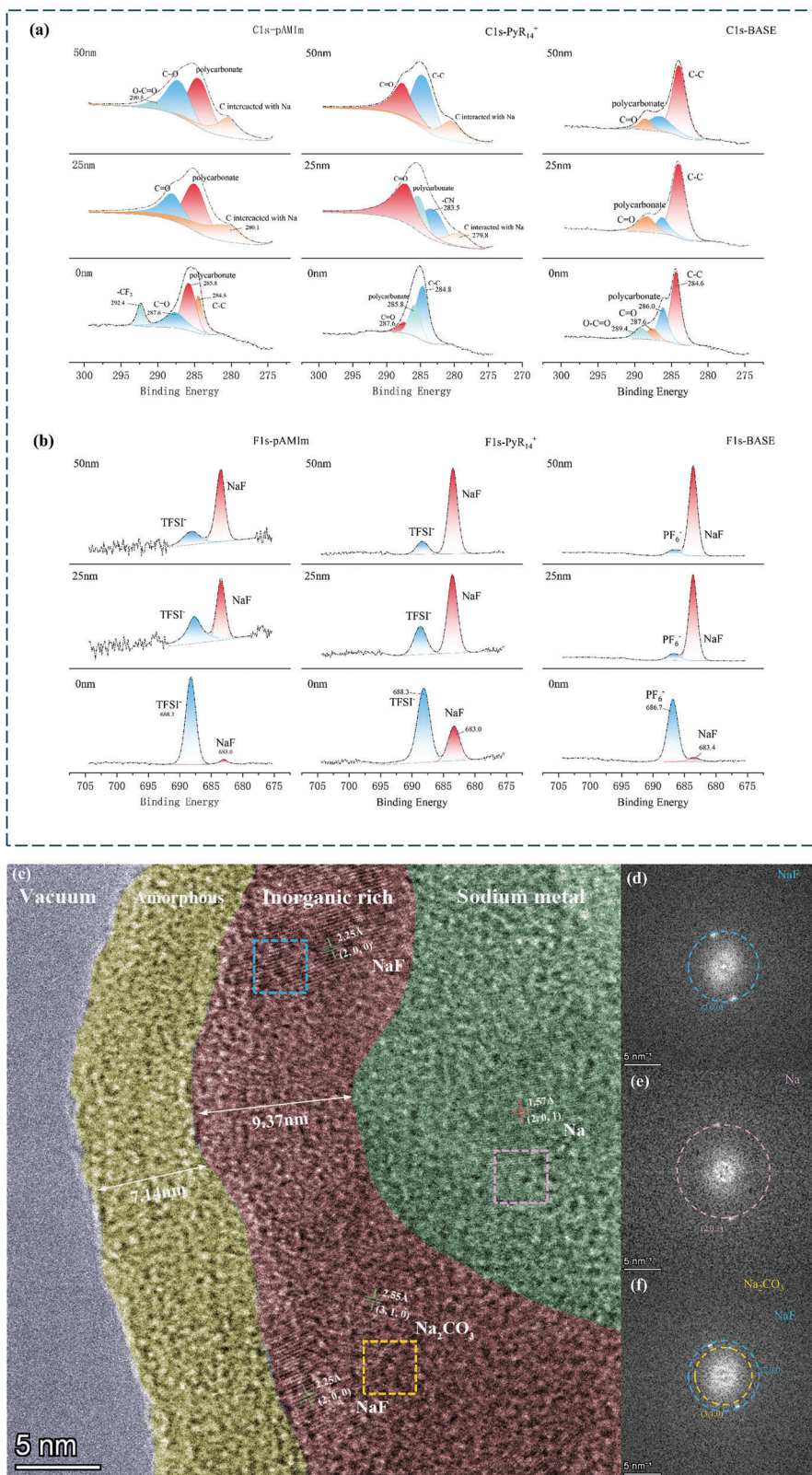MATERIALS**

www.afm-journal.de

Figure 6. a,b) C1s and F1s XPS etching analysis spectra from 0 nm to 50 nm of pAMIm, PyR14 PCGPE, and liquid electrolyte; c) HRTEM image showing the distribution of the SEI component from cryo-TEM characterization of sodium deposited on a copper mesh grid; d–f) FFT images of different areas of SEI.

**ADVANCED
SCIENCE NEWS**

www.advancedsciencenews.com

**ADVANCED
FUNCTIONAL
MATERIALS**

www.afm-journal.de

advancing sodium metal battery technology with enhanced safety and operational durability.

To enhance our understanding of the SEI layer in PCGPE, depth profiling X-ray photoelectron spectroscopy (XPS) was performed on the sodium surface of an NVP-sodium metal battery after 200 cycles at a 1 C rate. The analysis focused on the characterization of C1s and F1s spectral regions.

At the surface layer (0 nm), the C1s spectra predominantly displayed signals from organic species, including C—C, C=O, and polycarbonate structures. Notably, the sodium piece with pAMIm electrolyte showed a distinct -CF$_3$ signal, absent in the PyR14 electrolyte despite an equivalent amount of TFSI anions present. This suggests that the uneven SEI formation by PyR14 resulted in the exposure of a more inorganic-rich layer within the XPS observation area. At a deeper layer (25 nm), commercial electrolytes continued to show primarily organic species such as C—C and C=O, while the PCGPE signal revealed more sodium-related C signals. In the PyR14 electrolyte, a —CN signal indicative of succinonitrile leakage was detected, absent in the pAMIm sample. Further etching to 50 nm exposed a strong polycarbonate signal in the pAMIm electrolyte, while C—C signals were more pronounced in PyR14, suggesting that larger organic molecules in PyR14 are more stable and contribute to smoother SEI layers, reflecting a higher structural integrity and smoothness in pAMIm's SEI.

At the surface (0 nm), strong signals from TFSI and PF$_6$ anions were noted in both pAMIm and commercial electrolytes, with minimal NaF signal. However, PyR14's surface XPS showed smaller differences between TFSI anions and NaF signals, indicative of its irregular SEI film. As etching depth increased, the NaF signal strengthened while organic fluoride signals diminished, demonstrating the layered structure of the SEI with an outer amorphous layer and an inner layer rich in inorganic components. The N1s etching data, as shown in Figure S18 (Supporting Information), the similarities and differences between pAMIm PCGPE and PyR14 PCGPE can be concluded. At 0nm, the surface, the XPS N signal of the ionic liquid cations, and the N signal of the SN can be observed, both of which have similar signal types. However, as the etching progresses, inside the SEI layer, pAMIm PCGPE can observe the NaN3 signal, that is, the N signal of the inorganic substance, while only the SN signal can be observed in the PyR14 PCGPE pattern. This shows that the inner layer of SEI on the surface of PyR14 PCGPE corresponding to sodium tablets is still dominated by organic matter, which may also cause the uneven SEI on the surface of Na corresponding to PyR14 PCGPE.

Cryogenic electron microscopy (cryo-TEM) was employed to visually explore the SEI's structure and components. High-resolution cryo-TEM images showed an amorphous layer ≈7.14 nm thick near the vacuum interface, devoid of inorganic compound crystals. The inner part of this amorphous layer, ≈9.37 nm thick, was rich in inorganic compounds including NaF (Fm3m) and Na$_2$CO$_3$ (C12/m1), with deposited sodium metal at the innermost layer.[27] In the inorganic rich layer of SEI, there is a wide range of NaF, which has been shown to be an effective strategy for forming good SEI on the surface of sodium metal, so that the sodium metal and electrolyte can maintain good contact, improving the cycle's stability.[28] FFT transform images corresponding to NaF, Na$_2$CO$_3$, and sodium metal from **Figure 6**d–f

validated the crystalline structure within the rich-inorganic layer.

These findings provide a comprehensive view of the SEI structure in PCGPE, underscoring the superior stability and uniformity of the SEI in pAMIm-enhanced electrolytes, which contributes to the improved performance and safety of the associated sodium metal batteries.

3. Conclusion

This research successfully demonstrates significant advancements in the design and application of PCGPE through strategic polymer chain engineering and polycation crosslinking. These design choices have notably enhanced the ionic conductivity, electrochemical window, and cation transference number of the electrolyte. A straightforward film-forming method was employed to produce the electrolyte, which has proven effective in enabling stable charge–discharge cycling of NVP-sodium metal batteries. This method not only simplifies the manufacturing process but also ensures the production of a robust and functional electrolyte suitable for practical applications. In-depth investigations into the SEI layer on the sodium metal surface were conducted. These studies confirmed and detailed the SEI's structure, revealing an outer amorphous layer and an inner layer rich in inorganic components. Such detailed characterization helps in understanding the dynamics at the electrolyte-sodium metal electrode interface, which is crucial for optimizing battery performance and longevity. It should be noted, however, that the energy density of the cathode material chosen has a limit, which restricts the improvement of the energy density of the system. In this regard, future development may be based on the matching of various high specific energy cathodes materials, such as sulfur electrodes which have a higher specific capacity, or high voltage cathode materials such as Na$_2$Fe$_2$(SO$_4$)$_3$.[29]

Overall, this work not only showcases the enhanced electrochemical performance of the gel electrolyte but also deepens the understanding of the internal structure of the electrolyte and its interaction with the sodium metal electrode. The insights gained from theoretical calculations and advanced characterization techniques contribute significantly to the development of practical, high-performance sodium metal battery polymer gel solid electrolytes, marking a step forward in battery technology.

Supporting Information

Supporting Information is available from the Wiley Online Library or from the author.

Acknowledgements

Conflict of Interest

The authors declare no conflict of interest.

Data Availability Statement

The data that support the findings of this study are available on request from the corresponding author. The data are not publicly available due to privacy or ethical restrictions.

Keywords

[1] a) S. Chen, F. Dai, M. Cai, *ACS Energy Lett.* **2020**, *5*, 3140; b) G. Berckmans, M. Messagie, J. Smekens, N. Omar, L. Vanhaverbeke, J. Van Mierlo, *Energies* **2017**, *10*, 1314; c) C. Tang, W. Lu, Y. Zhang, W. Zhang, C. Cui, P. Liu, L. Han, X. Qian, L. Chen, F. Xu, Y. Mai, *Adv. Mater.* **2024**, *36*, 2402005.

[2] a) C. Vaalma, D. Buchholz, M. Weil, S. Passerini, *Nat. Rev. Mater.* **2018**, *3*, 18013; b) R. Usiskin, Y. Lu, J. Popovic, M. Law, P. Balaya, Y. S. Hu, J. Maier, *Nat. Rev. Mater.* **2021**, *6*, 1020; c) X. H. Liu, W. H. Lai, J. Peng, Y. Gao, H. Zhang, Z. Yang, X. X. He, Z. Hu, L. Li, Y. Qiao, M. H. Wu, H. K. Liu, *Carbon Neutr.* **2022**, *1*, 49; d) H. Wang, B. Yang, X. Z. Liao, J. Xu, D. Yang, Y. S. He, Z. F. Ma, *Electrochim. Acta* **2013**, *113*, 200; e) P. K. Nayak, L. Yang, W. Brehm, P. Adelhelm, *Angew. Chem., Int. Ed.* **2018**, *57*, 102; f) Z. Zheng, Y. Wang, Y. Zhang, X. Li, Y. Zhang, Y. S. He, H. Che, L. Li, Z. F. Ma, *Nano Energy* **2024**, *128*, 109907.

[3] a) X. Wang, C. Zhang, M. Sawczyk, J. Sun, Q. Yuan, F. Chen, T. C. Mendes, P. C. Howlett, C. Fu, Y. Wang, X. Tan, D. J. Searles, P. Král, C. J. Hawker, A. K. Whittaker, M. Forsyth, *Nat. Mater.* **2022**, *21*, 1057; b) Y. Zhao, K. R. Adair, X. Sun, *Energy Environ. Sci.* **2018**, *11*, 2673; c) M. Yang, F. Feng, Y. Ren, S. Chen, F. Chen, D. Chu, J. Guo, Z. Shi, T. Cai, W. Zhang, Z. F. Ma, S. Chen, T. Liu, *Adv. Funct. Mater.* **2023**, *33*, 2305383; d) H. Che, S. Chen, Y. Xie, H. Wang, K. Amine, X. Z. Liao, Z. F. Ma, *Energy Environ. Sci.* **2017**, *10*, 1075; e) W. Zhao, M. Guo, Z. Zuo, X. Zhao, H. Dou, Y. Zhang, S. Li, Z. Wu, Y. Shi, Z. Ma, X. Yang, *Engineering* **2022**, *11*, 87.

[4] a) B. Han, Y. Zou, Z. Zhang, X. Yang, X. Shi, H. Meng, H. Wang, K. Xu, Y. Deng, M. Gu, *Nat. Commun.* **2021**, *12*, 3066; b) H. Gao, S. Xin, L. Xue, J. B. Goodenough, *Chem* **2018**, *4*, 833.

[5] H. Wang, E. Matios, J. Luo, W. Li, *Chem. Soc. Rev.* **2020**, *49*, 3783.

[6] a) X. Chen, X. Shen, B. Li, H. J. Peng, X. B. Cheng, B. Q. Li, X. Q. Zhang, J. Q. Huang, Q. Zhang, *Angew. Chem., Int. Ed.* **2018**, *57*, 734; b) T. C. Mendes, X. Zhang, Y. Wu, P. C. Howlett, M. Forsyth, D. R. Macfarlane, *ACS Sustainable Chem. Eng.* **2019**, *7*, 3722; c) A. Hammami, N. Raymond, M. Armand, *Nature* **2003**, *424*, 635.

[7] a) S. Zhao, H. Che, S. Chen, H. Tao, J. Liao, X. Z. Liao, Z. F. Ma, *Electrochem. Energy Rev.* **2024**, *7*, 3; b) C. Zhao, L. Liu, X. Qi, Y. Lu, F. Wu, J. Zhao, Y. Yu, Y. S. Hu, L. Chen, *Adv. Energy Mater.* **2018**, *8*, 1703012; c) P. Pirayesh, E. Jin, Y. Wang, Y. Zhao, *Energy Environ. Sci.* **2024**, *17*, 442.

[8] a) H. Tang, Z. Deng, Z. Lin, Z. Wang, I. H. Chu, C. Chen, Z. Zhu, C. Zheng, S. P. Ong, *Chem. Mater.* **2018**, *30*, 163; b) B. N. Yun, S. Lee, W. D. Jung, H. J. Shin, J. T. Kim, S. Yu, K. Y. Chung, H. Kim, H. G. Jung, *ACS Appl. Mater. Interfaces* **2022**, *14*, 9242; c) G. Liu, J. Yang, J. Wu, Z. Peng, X. Yao, *Adv. Mater.* **2024**, *36*, 2311475.

[9] a) Z. Li, J. Fu, X. Zhou, S. Gui, L. Wei, H. Yang, H. Li, X. Guo, *Adv. Sci.* **2023**, *10*, 2201718; b) W. Ren, C. Ding, X. Fu, Y. Huang, *Energy Storage Mater.* **2021**, *34*, 515.

[10] a) Y. Ren, M. Yang, Z. Shi, J. Guo, D. Chu, F. Feng, H. Li, Z. F. Ma, S. Chen, T. Liu, *Energy Storage Mater.* **2023**, *61*, 102909; b) F. Gebert, J. Knott, R. Gorkin, S. L. Chou, S. X. Dou, *Energy Storage Mater.* **2021**, *36*, 10; c) D. Chen, M. Zhu, P. Kang, T. Zhu, H. Yuan, J. Lan, X. Yang, G. Sui, *Adv. Sci.* **2022**, *9*, 2103663.

[11] a) J. Pan, N. Wang, H. J. Fan, *Small Methods* **2022**, *6*, 2201032; b) F. Ahmad, A. Shahzad, S. Sarwar, H. Inam, U. Waqas, D. Pakulski, M. Bielejewski, S. Atiq, S. Amjad, M. Irfan, H. Khalid, M. Adnan, O. Gohar, *J. Power Sources* **2024**, *619*, 235221.

[12] M. Pigłowska, B. Kurc, M. Galiński, P. Fuć, M. Kamińska, N. Szymlet, P. Daszkiewicz, *Materials* **2021**, *14*, 6783.

[13] a) K. M. Harshlata, D. K. Rai, *Mater. Sci. Eng., B* **2021**, *267*, 115098; b) S. W. Chien, D. Safanama, S. S. Goh, N. Ding, M. Y. Tan, A. Y. X. Tan, D. W. H. Fam, *J. Energy Storage* **2024**, *89*, 111741; c) Z. Liu, Y. Du, H. Cui, L. Du, Z. Zhao, X. Wang, Z. Lv, M. Sun, Z. Liu, K. Li, G. Zhang, M. C. Lin, G. Cui, *J. Power Sources* **2021**, *497*, 229839.

[14] J. Luo, M. Yang, D. Wang, J. Zhang, K. Song, G. Tang, Z. Xie, X. Guo, Y. Shi, W. Chen, *Angew. Chem., Int. Ed.* **2023**, *62*, 202315076.

[15] B. Yavuzturk Gul, E. Pekgenc, V. Vatanpour, I. Koyuncu, *Carbohydr. Polym.* **2023**, *321*, 121296.

[16] a) L. Yuan, W. Jiang, *J. Appl. Polym. Sci.* **2021**, *138*, 50981; b) C. Regmi, J. Azadmanjiri, V. Mishra, Z. Sofer, S. Ashtiani, K. Friess, *Membranes* **2022**, *12*, 917.

[17] a) T. C. Nirmale, I. Karbhal, R. S. Kalubarme, M. V. Shelke, A. J. Varma, B. B. Kale, *ACS Appl. Mater. Interfaces* **2017**, *9*, 34773; b) S. S. More, N. D. Khupse, J. D. Ambekar, M. V. Kulkarni, B. B. Kale, *Energy Fuels* **2022**, *36*, 4999; c) R. B. Kale, S. S. More, N. D. Khupse, R. S. Kalubarme, M. V. Kulkarni, S. B. Rane, B. B. Kale, *Sustainable Energy Fuels* **2023**, *7*, 2934.

[18] S. Zhao, Y. Shen, H. Che, X. Z. Liao, X. M. Zhang, Z. F. Ma, *J. Membr. Sci.* **2024**, *702*, 122792.

[19] J. N. Sherwood, *The Plastically crystalline state : orientationally disordered crystals*, Wiley, Hoboken, New Jersey **1979**.

[20] a) P. J. Alarco, Y. Abu-Lebdeh, A. Abouimrane, M. Armand, *Nat. Mater.* **2004**, *3*, 476; b) M. J. Lee, J. Han, K. Lee, Y. J. Lee, B. G. Kim, K. N. Jung, B. J. Kim, S. W. Lee, *Nature* **2022**, *601*, 217; c) C. Wang, K. R. Adair, J. Liang, X. Li, Y. Sun, X. Li, J. Wang, Q. Sun, F. Zhao, X. Lin, R. Li, H. Huang, L. Zhang, R. Yang, S. Lu, X. Sun, *Adv. Funct. Mater.* **2019**, *29*, 1900392.

[21] a) İ. Uzun, *J. Polym. Res.* **2023**, *30*, 394; b) A. M. Hindeleh, D. J. Johnson, *Polymer* **1970**, *11*, 666.

[22] a) Z. Osman, *Ionics* **2005**, *11*, 397; b) L. Zubizarreta, M. Gil-Agusti, J. C. Espinosa, M. Garcia-Pellicer, A. Quijano-Lopez, *Mater. Plast.* **2021**, *58*, 237.

[23] a) X. Xia, W. M. Lamanna, J. R. Dahn, *J. Electrochem. Soc.* **2013**, *160*, A607; b) Y. Cao, T. Mu, *Ind. Eng. Chem. Res.* **2014**, *53*, 8651.

[24] a) M. J. Frisch, G. W. Trucks, H. B. Schlegel, G. E. Scuseria, M. A. Robb, J. R. Cheeseman, G. Scalmani, V. Barone, G. A. Petersson, H. Nakatsuji, X. Li, M. Caricato, A. V. Marenich, J. Bloino, B. G. Janesko, R. Gomperts, B. Mennucci, H. P. Hratchian, J. V. Ortiz, A. F. Izmaylov, J. L. Sonnenberg, Williams, F. D., F. Lipparini, F. Egidi, J. Goings, B. Peng, A. Petrone, T. Henderson, D. Ranasinghe, et al., *Gaussian 16 Rev. C.01*, Gaussian Inc, Wallingford, CT, USA **2016**; b) V. A. Rassolov, M. A. Ratner, J. A. Pople, P. C. Redfern, L. A. Curtiss, *J. Comput. Chem.* **2001**, *22*, 976; c) T. A. K. Roy Dennington, J. M. Millam, *GaussView, Version 6*, Semichem Inc, Shawnee Mission, KS, USA **2016**; d) J. D. Chai, M. Head-Gordon, *Phys. Chem. Chem. Phys.* **2008**, *10*, 6615.

[25] a) W. Humphrey, A. Dalke, K. Schulten, *J. Mol. Graph.* **1996**, *14*, 33; b) J. Eargle, D. Wright, Z. Luthey-Schulten, *Bioinformatics* **2006**, *22*,

**ADVANCED
SCIENCE NEWS**

www.advancedsciencenews.com

**ADVANCED
FUNCTIONAL
MATERIALS**

www.afm-journal.de

504; c) F. Neese, *WIREs Comput. Mol. Sci.* **2012**, *2*, 73; d) F. Neese, *WIREs Comput. Mol. Sci.* **2022**, *12*, e1606; e) S. Grimme, A. Hansen, S. Ehlert, J. M. Mewes, *J. Chem. Phys.* **2021**, *154*, 064103; f) T. Lu, F. Chen, *J. Comput. Chem.* **2012**, *33*, 580.

[26] a) M. Abraham, A. Alekseenko, V. Basov, C. Bergh, E. Briand, A. Brown, M. Doijade, G. Fiorin, S. Fleischmann, S. Gorelov, G. Gouaillardet, A. Grey, M. E. Irrgang, F. Jalalypour, J. Jordan, C. Kutzner, J. A. Lemkul, M. Lundborg, P. Merz, V. Miletic, D. Morozov, J. Nabet, S. Pall, A. Pasquadibisceglie, M. Pellegrino, H. Santuz, R. Schulz, T. Shugaeva, A. Shvetsov, A. Villa, *GROMACS 2024.2 Manual*, Zenodo **2024**; b) T. Lu, Sobtop, Version 1.0(dev4) **2024**; c) J. Wang, R. M. Wolf, J. W. Caldwell, P. A. Kollman, D. A. Case, *J. Comput. Chem.* **2004**, *25*, 1157.

[27] a) M. Dusek, G. Chapuis, M. Meyer, V. Petricek, *Acta Crystallogr. B* **2003**, *59*, 337; b) A. Jain, S. P. Ong, G. Hautier, W. Chen, W. D. Richards, S. Dacek, S. Cholia, D. Gunter, D. Skinner, G. Ceder, K. A. Persson, *APL Mater.* **2013**, *1*, 011002.

[28] X. Guo, Z. Xie, R. Wang, J. Luo, J. Chen, S. Guo, G. Tang, Y. Shi, W. Chen, *Angew. Chem., Int. Ed.* **2024**, *63*, 202402245.

[29] a) S. Murugan, S. V. Klostermann, P. Schützendübe, G. Richter, J. Kästner, M. R. Buchmeiser, *Adv. Funct. Mater.* **2022**, *32*, 2201191; b) L. Wen, J. Zhang, J. Zhang, L. Zhao, X. Wang, S. Wang, S. Ma, W. Li, J. Luo, J. Ge, W. Chen, *eScience* **2024**, 100313; c) Z. Zheng, X. Li, Y. Wang, Y. Zhang, Y. Jiang, Y. S. He, C. Niu, H. Che, L. Li, Z. F. Ma, *Energy Storage Mater.* **2025**, *74*, 103882.